nature physics

Supplementary information

https://doi.org/10.1038/s41567-024-02611-z

Emergence of fluctuating hydrodynamics in chaotic quantum systems

In the format provided by the authors and unedited

CONTENTS

I. EXPERIMENTAL DETAILS

A. Setup

The main experimental setup was described in Refs. [1, 2]. The experiment takes place in a glass cell with a large degree of optical access (see Fig. S1a). The atoms are vertically confined by loading them into a single plane of a shallow-angle vertical lattice (wavelength $\lambda = 1064\,\mathrm{nm}$, spacing $d = 8\,\mu\mathrm{m}$). In the horizontal plane, there is a square superlattice, consisting of two sets of retro-reflected bichromatic optical lattices. Each superlattice consists of a beam with wavelength $\lambda_{x,\mathrm{short}} = \lambda_{y,\mathrm{short}} = 767\,\mathrm{nm}$ (*short lattice*) and wavelength $\lambda_{x,\mathrm{long}} = \lambda_{y,\mathrm{long}} = 1534\,\mathrm{nm}$ (*long lattice*). The long lattice is frequency-locked to the short lattice, allowing us to freely vary the superlattice phase at the location of the atoms by introducing a frequency offset [3]. The lock is realized by frequency-doubling the light from the 1534 nm laser and beating it with the light from the short lattice laser. The beat signal is stabilized to a variable reference frequency via a phase-locked loop (Vescent D2-135), using the frequency-modulation piezo of the long lattice laser as the actuator.

The atomic configuration in the 2D lattice is read out using fluorescence imaging [2]. To this end, we freeze the configuration by quenching the horizontal lattices and the vertical lattice up to a depth of around 400 µK. We then turn on optical molasses cooling on the D2 line ($\lambda = 852\,\mathrm{nm}$), which causes the atoms to scatter fluorescence photons and at the same time cools them in their respective lattice site. The scattered fluorescence photons are collected using a high-resolution objective (NA = 0.8) and focused onto a sCMOS camera (Teledyne Photometrics Kinetix) with a magnification of around 40. In addition to the imaging, we use the objective to project arbitrary repulsive potentials onto the atoms by imaging the surface of a digital micromirror device (DMD, Texas Instruments DLP6500, interface by bbs Bild- und Lichtsysteme GmbH). The DMD is illuminated by light coming from a multi-mode diode laser, which emits at a wavelength of $\lambda = 525\,\mathrm{nm}$ and has a spectral width of several nanometers (Wavespectrum WSLX525-005-400M-H), resulting in a low coherence to reduce any interference speckle pattern.

B. Initial state preparation and experimental sequence

The experimental sequence is depicted in Fig. S1b. We prepare the initial state by loading a rectangular Mott insulator in a repulsive box potential. To this end, we start with a 2D cloud of ^{133}Cs atoms confined in a single plane of the vertical lattice. The horizontal confinement is provided by projecting a repulsive box using the DMD. Before adding the horizontal lattices, the phase of the superlattice in x-direction, which we use to prepare the initial state, is chosen to realize an array of strongly tilted double wells at the position of the atoms (see Fig. S1a) [4]. To prepare the rectangular Mott insulator, we ramp up the superlattice in the x-direction as well as the short lattice in the y-direction using a two-step sigmoidal ramp deep into the Mott insulating regime with a total duration of 320 ms. Additionally, we ramp the offset field from 22.6 G to 33 G in order to increase the scattering length from $a = 280a_0$ to $a = 680a_0$, where a_0 is the Bohr radius. To avoid doublon generation, we choose the height of the box to be around $U/2$, causing excess atoms to spill over the central region when crossing the transition. This allows us to realize rectangular Mott insulating states with a filling of typically 84(8)% in the even and 4(3)% in the odd rows. At this point, the density distribution is frozen out, realizing the initial state that resembles a 1D charge density wave (CDW, see Fig. S1d).

In preparation for the quench experiment, we first increase the height of the DMD walls to $\sim 5\,U$ in order

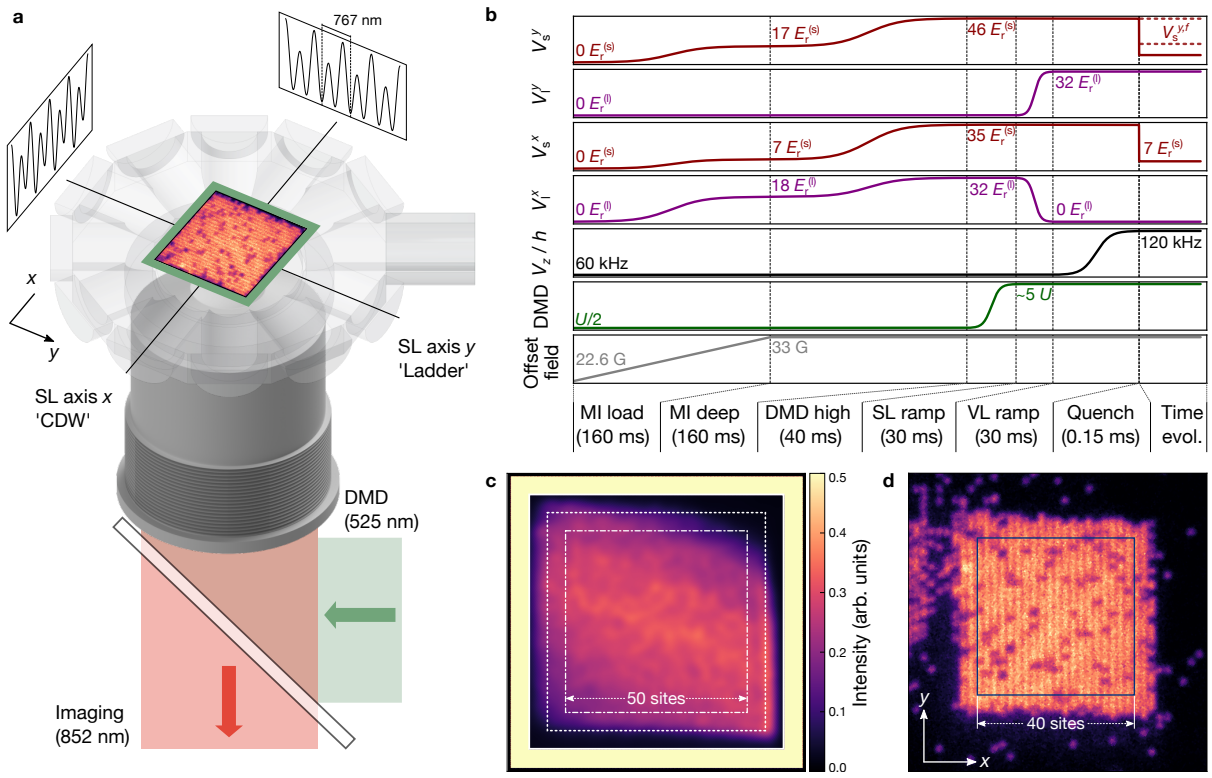

Figure S1. **Experimental setup and sequence.** **a**, Sketch of the experimental setup illustrating high-resolution imaging, superlattice configuration, and DMD. Drawing not to scale. **b**, Experimental sequence. The depths of the short and long horizontal lattices V_i^j are given in terms of their respective recoil energies. $V_s^{y,f}$ is the final depth of the short lattice in y-direction that is chosen to realize a specific $J_\perp$. **c**, Flattening mask as obtained in the iterative potential compensation algorithm. The mask is projected onto the atomic plane with the DMD to compensate the external harmonic confinement. The dashed square denotes the 60×60 site region used for the compensation algorithm, and the dash-dotted square is the 50×50 region used in the experiment. **d**, For data evaluation, we use a 40×40 sites ROI inside the 50×50 sites flat box potential. Shown is a single fluorescence image of the CDW initial state.

to prevent atoms from tunneling into or out of the box region. Furthermore, in order to prepare long ladder systems, we completely remove the long lattice along the x-direction and simultaneously ramp up the long lattice in the y-direction to $17\,E_\mathrm{r}^{(\mathrm{l})}$, where $E_\mathrm{r}^{(\mathrm{l,s})} = h^2/(2m\lambda_{(\mathrm{l,s})}^2)$ is the recoil energy in the short and long horizontal lattice, respectively. The depth of the long lattice is chosen sufficiently large so that tunneling between neighbouring ladders is suppressed. Finally, the vertical lattice is increased to a depth of $V_z/h = 120\,\mathrm{kHz}$ to further increase the interaction energy during the time evolution. This moves the system deeper into the hard-core limit and ensures that the doublon fraction stays negligibly small ($\lesssim 3\%$ of doubly occupied sites) for all values of $J_\perp/J$.

The time evolution is turned on by quenching the short lattice along the x-direction down to $7\,E_\mathrm{r}^{(\mathrm{s})}$ over $150\,\mu\mathrm{s}$, corresponding to a tunnel coupling of $J/h = 96(3)\,\mathrm{Hz}$. When studying the equilibration in ladder systems, we quench the short lattice along the y-direction at the same time to realize a specific value of $J_\perp$. The tunnel couplings J and $J_\perp$ have been calibrated using parametric heating resonances and tunnelling oscillations in isolated double wells, respectively.

C. On-site interaction energy

We estimate the on-site interaction energy U using two independent methods: (1) measuring the fraction of doublons in the ladder ground state for different coupling ratios $J_\perp/J$ and (2) spectroscopically probing low-energy excitations in the systems, which leads to the formation of doublons and provides a lower bound for the on-site Hubbard interaction, as discussed below.

To prepare the ground state in coupled ladders, we first prepare a Mott insulator in the short-spaced lattices ($n = 1$) and then ramp up (down) the long (short) lattices in 50 ms to the final experimental parameters corresponding to separated ladder systems with $J_\perp/J \approx 0.0, 0.5, 1.0$. We find a mean filling (subject to parity projection) of $0.95(3), 0.91(3)$ and $0.85(3)$ for the three cases, respectively, normalized to the mean filling of the Mott insulating state. Comparing these values with exact small-scale diagonalization numerics for the ground state suggests

that $U/J \simeq 13, 11$, and 11 for $J_\perp/J \approx 0.0, 0.5, 1.0$. This comparison assumes perfect filling, no on-site disorder, and was carried out for small system sizes of up to 12 sites.

Additionally, we provide a lower bound for U using modulation spectroscopy by preparing the ground state as described above, followed by a modulation of the lattice potential using a running-wave lattice, as introduced in Ref. [5]. The modulation takes 40 ms with a weak amplitude of about $0.01U$. We measure atom loss as a function of modulation frequency and find a resonance associated with U. Fitting the resonance using a Gaussian, we obtain $U/J = 9.5(2), 8.4(2), 7.5(2)$ for $J_\perp/J \approx 0.0, 0.5, 1.0$. However, these values likely underestimate the real value of U/J, since the modulation does not correspond to a pure excitation of localized doublons. The finite ratio of U/J leads to states in the many-body spectrum at energies significantly smaller than U, since doublons can lower their energy by delocalizing across the system. The energy gap between the ground state and the first excited state for our parameters can be up to 30% smaller (based on exact diagonalization calculations for small system sizes). Hence, the observed heating resonances only provide a lower bound for the ratio U/J.

Most importantly, both results show that our experiments are carried out in the regime of hard-core bosons.

D. Potential flattening

To observe spatially homogeneous dynamics, we correct for external confinement within the repulsive box potential using an iterative potential compensation algorithm. To this end, we prepare a cold superfluid in the box, as its density distribution is particularly sensitive to potential corrugations. The first compensation mask is generated by dividing the mean occupation averaged over the entire box region by the measured spatial distribution of atoms averaged over ten repetitions. Using a PI-controlled feedback loop, this procedure is typically repeated over ten iterations, where each step gradually improves the compensation mask from the previous step. A typical compensation mask is shown in Fig. S1c, suggesting that the external confinement has a dominant contribution that is orientated diagonally with respect to the lattice axes. We can attribute this profile to the in-plane confinement of the shallow-angle vertical lattice. To avoid edge effects occurring close to the border of the compensation region, we perform the compensation algorithm using a box region that is significantly larger compared to the 50×50 sites box that we employ in the experiment.

E. Reconstruction of the lattice occupation

Using high-resolution fluorescence imaging on the D2 line, we achieve a resolution of about 850 nm. To resolve atoms in the short lattice with spacing $a = 383.5$ nm, which is less than half the imaging resolution, we employ a reconstruction algorithm based on a convolutional neural network trained directly with experimental data [2]. We estimate that this allows us to determine the occupation with a fidelity of at least 96% [2].

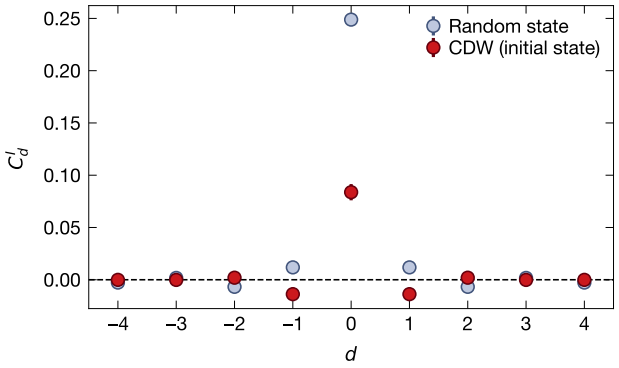

Figure S2. **Calibration measurements for detecting systematic errors in the single-site reconstruction.** Spatial correlation profile C_d^I of a charge density wave with high imbalance ~ 0.9 and a random state with near-zero imbalance. The profiles have been obtained from about 40 and 70 fluorescence images, respectively. Error bars represent the standard deviation.

II. DATA ANALYSIS

A. Post-selection on atom number

We use a 40×40 sites large region of interest (ROI) in the flat box potential region containing 50×50 sites. The ROI is chosen such that there is a buffer of around five sites between the ROI and the edges of the box region (see Fig. S1d). A small percentage of fluorescence images contain few or no atoms due to errors in the sequence execution. We remove these shots based on the average filling n in the ROI, using $\bar{n} = 0.36$ as a threshold value. After this procedure, the average filling in the ROI is $\bar{n} = 0.43(2)$.

B. Density-density correlations

The (two-point) density-density correlators are defined as

$$C_d^{\alpha,\beta} = \langle \hat{n}_{\alpha,i} \hat{n}_{\beta,j} \rangle - \langle \hat{n}_{\alpha,i} \rangle \langle \hat{n}_{\beta,j} \rangle \tag{S1}$$

where $\alpha, \beta = 1, 2$ denote the legs of the ladder and i, j are indices of sites at distance $d = i - j$ in the respective legs of the ladder. The average $\langle \ldots \rangle = \langle \langle \ldots \rangle_k \rangle_d$ is first taken over all ladders (index k) in all fluorescence images

and then over all combinations of indices leading to the same distance $d = i - j$.

In our ladder geometry, it is possible to compute three different kinds of density-density correlators.

- If $\alpha = \beta$, we calculate the correlations along the 1D chains

$$C_d^I = \frac{1}{2}\left(C_d^{1,1} + C_d^{2,2}\right). \tag{S2}$$

- Secondly, we can compute the correlations between the legs of the ladder along the direction of the chains:

$$C_d^{II} = \frac{1}{2}\left(C_d^{2,1} + C_d^{1,2}\right). \tag{S3}$$

- Lastly, one can consider the ladder as a quasi one-dimensional system and compute the correlations of the total atom number in the rungs of the ladder:

$$\begin{aligned} C_d^{III} &= 2\left(C_d^I + C_d^{II}\right) \\ &= \langle \hat{N}_i \hat{N}_j \rangle - \langle \hat{N}_i \rangle \langle \hat{N}_j \rangle, \end{aligned} \tag{S4}$$

where $\hat{N}_i = \hat{n}_{1,i} + \hat{n}_{2,i}$. In the main text, we make use of this correlator as it provides us with the highest signal-to-noise ratio when studying the details of the post-quench dynamics. Further, it is a natural choice for investigating the transition from a (quasi-one-dimensional) ladder system to a (truly one-dimensional) system of decoupled chains.

C. Correcting systematic errors in the single-site reconstruction

Due to the finite fidelity of our reconstruction algorithm, there may be correlated errors that impact the measured short-distance correlations, presumably on the order of $1-\mathcal{F}$, where $\mathcal{F}$ is the fidelity of the reconstruction process [2, 6]. This is because the reconstruction errors are not entirely random but are more likely to occur for certain occupation patterns. For example, the presence of an atom in a particular site might enhance the probability that the reconstruction algorithm will detect an atom on the adjacent site even if there is no atom.

In order to investigate whether these artificial correlations occur, we perform two calibration measurements for two different states with different imbalances that can be assumed to lack any density-density correlations for $|d| > 0$. The two states are:

- the CDW in the initial state before the quench with filling $\bar{n}_{\text{initial}} = 0.44(2)$ and imbalance $\mathcal{I}_{\text{initial}} = 0.91(7)$, prepared by adiabatically ramping up a tilted superlattice, and
- a random state with filling $\bar{n}_{\text{random}} = 0.48(2)$ and imbalance $\mathcal{I}_{\text{random}} = 0.00(13)$, prepared by taking an $n = 1$ Mott insulator in the short lattices and removing about half of the atoms using microwave addressing and a blow-out pulse.

Fig. S2 shows the density-density correlations C_d^I measured in these two states as a function of distance $d = i - j$. Since we do not expect to find any non-zero density-density correlations for $|d| > 0$, the visible deviations from zero, particularly for $|d| = 1, 2$, have to be attributed to an artefact of the reconstruction process with sign and strength depending on the imbalance. In order to correct the data for this artefact, we compute an imbalance-dependent correction by interpolating between the spatial correlation profiles of the two calibration measurements. We assume that this interpolation is linear, neglecting any (small) non-linear effects.

For the imbalance $\mathcal{I}_{\text{initial}}$ of the initial state, we measure a correlation profile $\mathbf{C}_{\text{initial}}$, while for the random state with the imbalance $\mathcal{I}_{\text{random}}$, we measure a correlation profile $\mathbf{C}_{\text{random}}$ (each component corresponds to a distance $d = i - j$).

We obtain the corrected correlations

$$\mathbf{C}_{\text{corrected}} = \mathbf{C}_{\text{measured}} - \mathbf{C}_{\text{correction}}(\mathcal{I}) \tag{S5}$$

by subtracting the imbalance-dependent correction $\mathbf{C}_{\text{correction}}(\mathcal{I})$ from the measured correlations $\mathbf{C}_{\text{measured}}$. Assuming that the correction depends linearly on the imbalance $\mathcal{I}$, we can construct the correction from the calibration measurements as follows:

$$\mathbf{C}_{\text{correction}}(\mathcal{I}) = \mathbf{C}_{\text{random}} + \frac{\mathcal{I}}{\mathcal{I}_{\text{initial}}}\left(\mathbf{C}_{\text{initial}} - \mathbf{C}_{\text{random}}\right). \tag{S6}$$

Similarly, we can find a correction for C_d^{II} and C_d^{III}. Note that the correction is only applied for $|d| = 1, 2$, i.e., for distances that are likely to be affected by reconstruction-caused density-density correlations due to the point spread function (PSF) of an atom leaking into other sites up to two sites away. This is supported by the spatial profile in Fig. S2, which shows the artificial correlations dropping quickly to zero within distance two. For C_d^{II}, we additionally correct $d = 0$ as $C_{d=0}^{II}$ is the density-density correlation between two adjacent sites on different legs of the ladder, corresponding to a real-space distance of one. The correlation cones before and after applying the correction are shown in Fig. S3. In particular, Fig. S3b (centre column) shows how the C_d^{II} correlations grow when $J_\perp/J > 0$ is increased and the two legs of the ladders start interacting with each other. In contrast, for $J_\perp = 0$ we measure approximately $C_d^{II} = 0$.

D. Computing variances from density-density correlations

The atom number variance in a ladder subsystem of size $2 \times L$ is closely related to the correlators $C_{i,j}^{\alpha,\beta}$ evaluated at distances $|d| < L$. By expanding the definition of

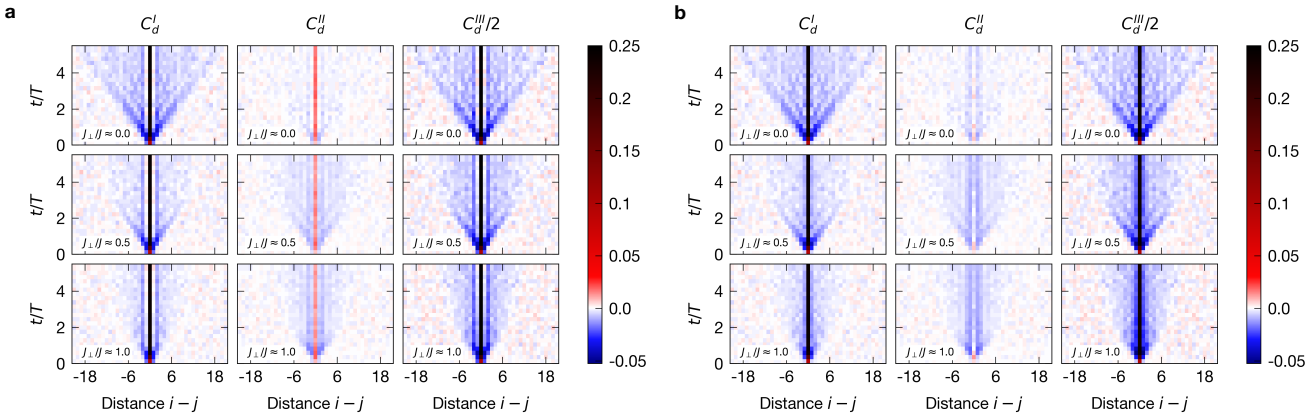

Figure S3. **Impact of the reconstruction correction on the density-density correlations.** Density-density correlations along the legs of the ladder (C_d^I, left column), between the legs of the ladder (C_d^{II}, centre column) and correlations along the ladder of atom numbers summed in the rungs (C_d^{III}, right column) for $J_\perp/J \approx 0.0, 0.5, 1.0$ (top, centre and bottom row, respectively) as a function of distance $d = i - j$ and evolution time t. **a**, Before the correction described in Section II C. **b**, After the correction described in Section II C.

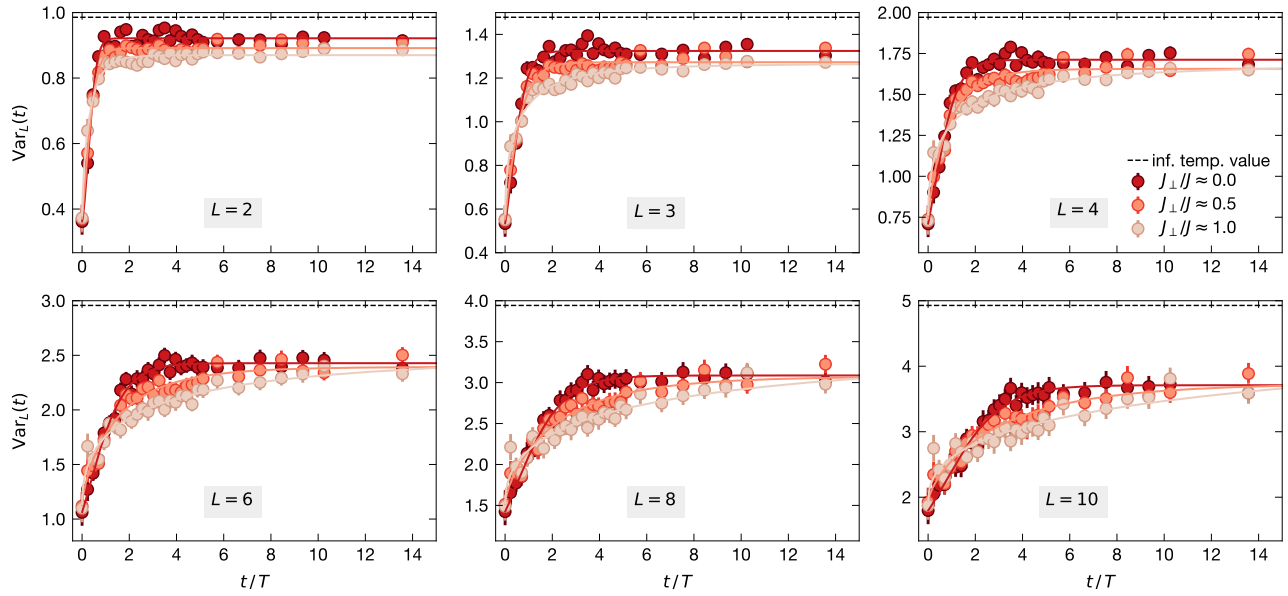

Figure S4. **Variance growth for different subsystem sizes L and $J_\perp/J \approx 0.0, 0.5, 1.0$.** Solid curves are the fits using the empirical fit function in equation (S11).

the atom number variance in a ladder subsystem of size $2 \times L$ we find that:

$$\begin{aligned}\mathrm{Var}_L(t) &= \left\langle (\hat{n}_{1,1} + \hat{n}_{2,1} + \cdots + \hat{n}_{1,L} + \hat{n}_{2,L})^2 \right\rangle \\ &\quad - \left\langle \hat{n}_{1,1} + \hat{n}_{2,1} + \cdots + \hat{n}_{1,L} + \hat{n}_{2,L} \right\rangle^2 \\ &= \sum_{i,j=1}^{L} \left(C_{i,j}^{1,1} + C_{i,j}^{1,2} + C_{i,j}^{2,1} + C_{i,j}^{2,2} \right).\end{aligned} \tag{S7}$$

The sums in this expression can be further expanded showing directly the connection to the correlation cone. For instance:

$$\begin{aligned}\sum_{i,j=1}^{L} C_{i,j}^{1,1} &= L\, C_0^{1,1} + 2\,(L-1)\, C_1^{1,1} \\ &\quad + 2\,(L-2)\, C_2^{1,1} + \cdots + 2\, C_{L-1}^{1,1}.\end{aligned} \tag{S8}$$

In the limit of decoupled 1D chains ($J_\perp/J = 0$), $C_{i,j}^{1,2} = C_{i,j}^{2,1} = 0$ and the variance of the $2 \times L$ subsystem is just a sum of variances of the two $1 \times L$ subsystems.

Although we cannot easily correct the real-space densities $\hat{n}_{\alpha,i}$ for the reconstruction artefact, we can correct

the correlations (see Section II C) and therefore the atom number variances.

E. Determination of the diffusion constant

In the chaotic limit ($J_\perp/J = 1$), we find that the fluctuation growth is diffusive. For initial states, ρ that are diagonal in the number basis, the density-density correlator $C_d^{\alpha,\beta}$ takes the following form within MFT (see Section IV A for a detailed derivation):

$$C_d^{\alpha,\beta} = (\langle \mathrm{Var}(\hat{n}_{\alpha,j})\rangle_{\alpha,j} - \chi(\overline{n}))\frac{a\, e^{-\frac{d^2a^2}{8Dt}}}{2\sqrt{8\pi Dt}} + \chi(\overline{n})\delta_{\alpha,\beta}\delta_{d,0}, \tag{S9}$$

where $\overline{n}$ is the average occupation (filling) in the initial state, $\chi(n) = n(1-n)$ is the susceptibility, and $\langle \mathrm{Var}(\hat{n}_{\alpha,j})\rangle_{\alpha,j}$ is the spatial average of the number variance $\mathrm{Var}(\hat{n}_{\alpha,j})$ in the initial state. In this expression, D denotes the equilibrium diffusion constant, d is the distance along the ladder between lattice site i in leg α and lattice site j in leg β in units of the lattice spacing a. The correlations as a function of distance and time form a cone of a Gaussian shape with a width that increases with time as $\sigma_c(t) = \sqrt{4Dt/a^2}$.

To obtain the diffusion constant from our experimental data, we use a simplified form of the expression in equation (S9), which includes an offset parameter c,

$$C_d^{III} = \sum_{\alpha,\beta=1,2} C_d^{\alpha,\beta} = A\frac{a\, e^{-\frac{d^2a^2}{8Dt}}}{2\sqrt{8\pi Dt}} + c \tag{S10}$$

and fit the measured correlations C_d^{III} for $1 \le d \le 20$ and all time data points with free parameters A, D and c. The result of the fit, which yields $D = 0.88(5)\, Ja^2/\hbar$, is shown in Fig. 5.

F. Fitting the number variance time evolution

To characterize the variance growth, we fit all variance-time evolution curves using the following empirical fit function:

$$\mathrm{Var}(t, \mathrm{Var}_\infty, k, d) = (\mathrm{Var}_\infty - \mathrm{Var}_0)\left(\frac{2}{1+e^{-kt^d}} - 1\right) + \mathrm{Var}_0, \tag{S11}$$

where $\mathrm{Var}_0 = \mathrm{Var}(t=0)$ and $\mathrm{Var}_\infty = \mathrm{Var}(t\to\infty)$. The free fit parameters are Var_∞, d and k, while Var_0 is fixed to the variance measured at $t = 0$. Fig. S4 shows the atom number variance as a function of evolution time t and subsystem size L for $J_\perp/J \approx 0.0, 0.5, 1$. The solid lines are the fits using equation (S11). For the thermalisation of an infinite temperature state, the observed saturation values should equal $2L\bar{n}(1-\bar{n}) = L/2$ for an infinite system and a perfect initial state with $\bar{n} = 1/2$. However, due to residual errors after correcting systematic reconstruction errors (see Section II C), the presence of disorder (see Section III B), finite size effects (see Section III C) and reduced filling $\bar{n} < 1/2$, we expect the atom number variance to saturate at lower levels.

To quantify the timescale of variance growth, we determine the intersection of the fit result with a threshold value of 80% of the fitted saturation value (i.e., 0% corresponds to Var_0 and 100% is equivalent to Var_∞), which defines the saturation time t_{sat}. The uncertainty of t_{sat} is obtained by evaluating the inverse of equation (S11) at t_{sat}, taking into account the uncertainties of all fitted variables. The saturation time t_{sat} and its scaling with increasing system size is plotted in Figs. 3b, c of the main text.

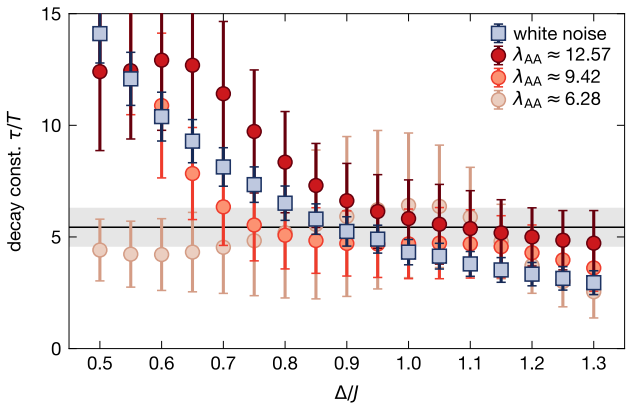

Figure S5. **Estimation of the disorder strength.** Result of an exponentially damped Bessel fit to the simulated imbalance oscillations for white noise disorder and Aubry-André disorder of three different periods λ_{AA} (in units of lattice sites) and different disorder amplitudes. The error bars are the fit error bars. The black line with the shaded region shows the experimentally measured damping constant τ and its uncertainty.

III. BENCHMARKING OF EXPERIMENTAL IMPERFECTIONS

A. Free-fermion approach

We have performed numerical simulations of one-dimensional chains to understand the role of experimental imperfections, such as disorder, quality of the initial state, and finite system size effects. Hard-core bosons in one dimension can be mapped onto spinless fermions using the Jordan-Wigner transformation: It states that the bosonic creation and annihilation operators $\hat{a}_i^\dagger$ and $\hat{a}_i$ that satisfy the commutation relation $\left[\hat{a}_i, \hat{a}_j^\dagger\right] = \delta_{i,j}$ can be replaced by corresponding fermionic operators $\hat{c}_i^\dagger$ and

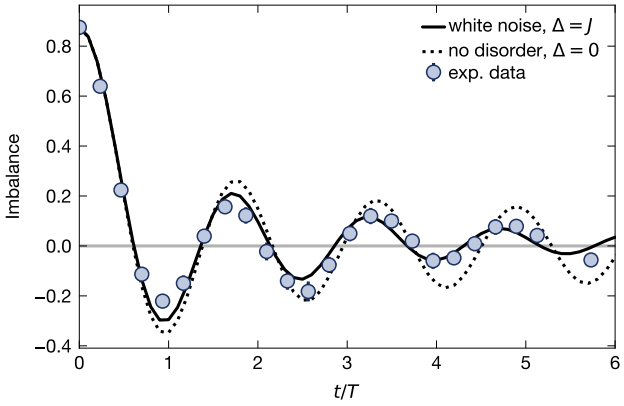

Figure S6. **Effect of disorder on the imbalance.** Free-fermion simulations of imbalance oscillation for systems without disorder (dotted line) and white-noise disorder of amplitude $\Delta = J$ (solid line) for which we found reasonable agreement with the experimental data.

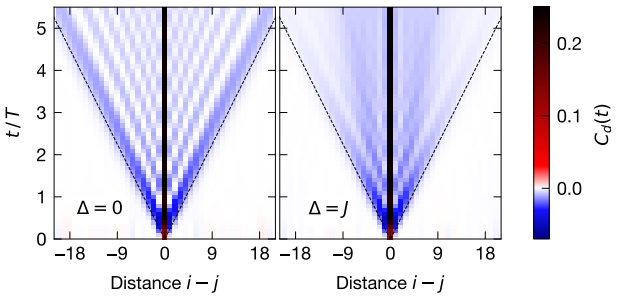

Figure S7. **Effect of disorder on correlation spreading.** Ballistic correlation cones calculated using the free-fermion simulation for an imperfect initial state and cases with no disorder ($\Delta = 0$) and white noise disorder $\Delta = J$. Disorder reduces the visibility of the outer arm of the cone at larger distances and leads to smearing of the correlations, hiding the internal structure of the correlation cone. The dashed line indicates the Lieb-Robinson velocity $4Ja/\hbar$.

$\hat{c}_i$ that fulfil $\left[\hat{c}_i, \hat{c}_j^\dagger\right]_+ = \delta_{i,j}$. The resulting Hamiltonian reads

$$\hat{H}_{\mathrm{ff}} = -J\left(\sum_i \hat{c}_i^\dagger \hat{c}_{i+1} + \mathrm{h.c.}\right) + \sum_i V_i \hat{n}_i, \tag{S12}$$

where V_i is the potential energy at site i. Note that the interaction term has dropped out.

For a perfectly homogeneous (i.e., disorder-free) infinite one-dimensional system and a defect-free initial state, the imbalance and the connected density-density correlator will evolve in time according to [7]:

$$\mathcal{I}(t) = \mathcal{J}_0\left(4tJ/\hbar\right), \tag{S13}$$

$$\langle \hat{n}_j(t)\hat{n}_k(t)\rangle - \langle \hat{n}_j(t)\rangle \langle \hat{n}_k(t)\rangle = \frac{1}{4}\delta_{j,k} - \frac{1}{4}\mathcal{J}_{j-k}(4tJ/\hbar)^2 \tag{S14}$$

where $\delta_{j,k}$ is the Kronecker delta and $\mathcal{J}_m$ is the mth-order Bessel function of the first kind.

For non-zero on-site potential terms (such as disorder potential), an imperfect initial state, and finite system size, we do not have such analytic predictions. Following the calculation outlined in [7], we obtain expressions for $\langle \hat{n}_j(t)\rangle$ and $\langle \hat{n}_j(t)\hat{n}_k(t)\rangle$ in terms of the time evolution operator $\hat{U}(t) = e^{-i\hat{H}_{\mathrm{ff}}t/\hbar}$. This operator is then computed numerically and gives us access to on-site occupations, two-point density-density correlators and therefore also atom number variances (see SM Section II B).

B. Disorder and initial state quality

As described in Section I D, we remove the large-scale harmonic confinement using a potential compensation algorithm. Thus, we assume that the remaining inhomogeneities are caused by disorder in the form of random potential corrugations. To investigate the impact of disorder on our experimental results, estimate the disorder strength, and see whether it can explain our experimental observations, we compare our measurements for $J_\perp/J \approx 0.0$ with results obtained from one-dimensional free-fermion simulations (see Section III A). We consider both white noise and Aubry-André-type disorder, exploring the impact of random (uncorrelated) and deterministic disorder potentials, respectively. For the white noise disorder model, V_i in equation (S12) is randomly sampled from the interval $[-\Delta, \Delta]$. For Aubry-André disorder, $V_i = \Delta \sin\left(2\pi i/\lambda_{\mathrm{AA}} + \phi\right)$, where λ_{AA} is the period of the periodic wave potential in units of lattice sites and ϕ is its phase that is randomly sampled from the interval $[0, 2\pi]$. In both cases, Δ denotes the disorder amplitude. Although it is unclear exactly what type of disorder governs our system, comparing the impact of the two disorder models allows us to obtain an estimate for Δ, as shown below.

The free-fermion simulation is performed on a one-dimensional lattice of length $N = 50$ sites and with open boundary conditions. Similarly to the experiment, we use a ROI of 40 sites for evaluation, leaving a buffer zone of 5 sites between the edges of the ROI and the edge of the overall system. We compute the time evolution of 600 initial states that are randomly sampled using the experimentally measured fillings of the odd and even sites (see SM Section I A).

In order to estimate the disorder strength in our experiment, we fit the decay constant τ of the simulated imbalance oscillations and compare it to the experimentally measured one (see Fig. 3a). Fig. S5 shows the fitted decay constants as a function of disorder strength for both white noise disorder and Aubry-André disorder of selected wavelengths. We find that the measured imbal-

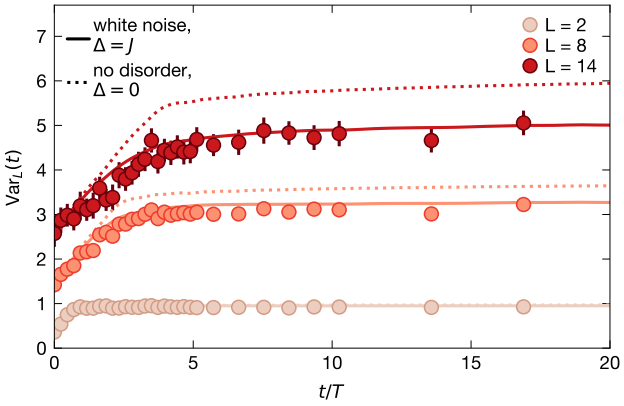

Figure S8. **Effect of disorder on the variance growth.** Experimentally measured atom number variances in subsystems of size $L = 2, 8$ and 14 ($J_\perp/J = 0$) and respective free-fermion predictions that have been calculated from the correlation cones shown in Fig. S7. The solid lines show the white noise $\Delta = J$ prediction, while the dotted lines show the zero disorder prediction. Disorder affects the dynamics for $t \gtrapprox 2T$, effectively reducing the variance growth and saturation value. Variance at $t = 0$ is non-zero due to the initial state quality.

ance decay constant is consistent with disorder strength $\Delta \sim J$ with some dependence on the disorder model. Assuming white noise disorder of strength $\Delta = J$, we find good agreement with the experimental imbalance oscillations, as highlighted in Fig. S6. Fig. S7 shows how the presence of disorder reduces the contrast of the correlation cone, hiding its inner structure and reducing the visibility of the outer arm. However, the spreading velocity, as indicated by the outer edge, remains unaffected.

Fig. S8 shows that white noise disorder of amplitude $\Delta \approx J$, independently benchmarked using the imbalance oscillations, leads to an excellent agreement with the experimentally measured atom number variances.

Using the free-fermion simulation and the approach outlined in [8], we can estimate the Anderson localisation length corresponding to our white noise disorder strength. For a disorder amplitude of $\Delta \approx J$, we obtain the localisation length of approximately 18 lattice sites, which is larger than the subsystem sizes that we use to study fluctuations in the ballistic case ($J_\perp/J = 0$).

C. Impact of finite system size effects

In this section, we investigate the impact of finite system size effects, in particular the impact on the saturation value of the atom number variance, using both simulations and experimental data.

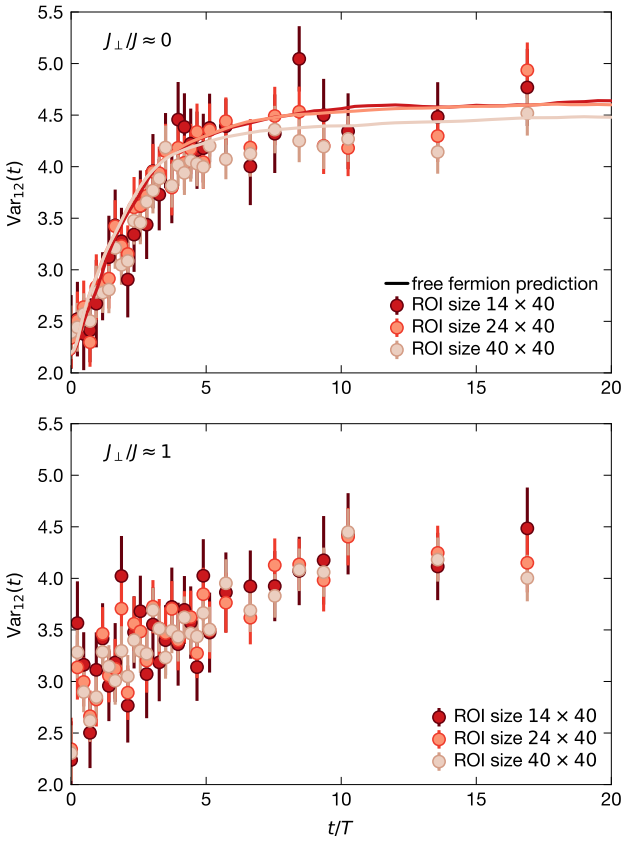

Figure S9. **Edge effects for $J_\perp/J \approx 0.0, 1.0$.** Variance growth for subsystem size $L = 12$ evaluated for three different ROI sizes: 12×40, 20×40 and 40×40 sites (full ROI, see Fig. 2). Solid lines show the free-fermion prediction for $J_\perp/J \approx 0$ with white noise disorder $\Delta = J$ evaluated for the same ROI sizes and overall system size 50.

1. *Experimental data*

In order to ensure that the choice of our 40×40 sites ROI inside the full 50×50 system does not introduce significant finite-size effects, we compare the data evaluation in central ROIs of three different sizes. Fig. S9 shows the time evolution of the atom number variance in a subsystem of size $L = 12$ for the three different ROIs, 14×40, 24×40 and 40×40 sites for $J_\perp/J \approx 0.0$ and 1.0. In both cases, the three curves for different ROI sizes agree within error bars. Thus, we conclude that the reduction of the variance saturation value compared to the infinite-temperature expectation is not a consequence of our large ROI, which we have chosen for the sake of better statistics.

2. *Simulations of decoupled 1D chains*

We perform a free-fermion simulation for system sizes 50 and 250 for cases without disorder and disorder of

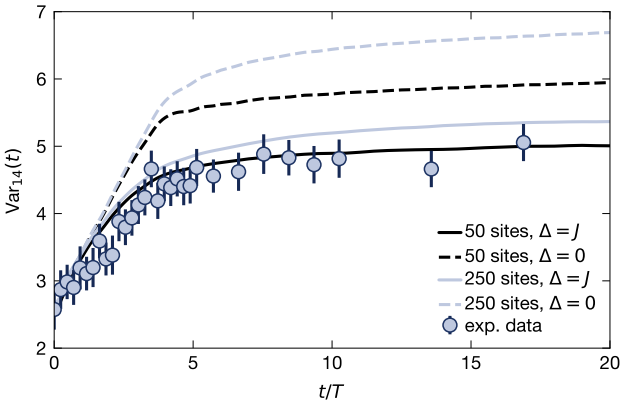

Figure S10. **Combined effect of finite system size and disorder for $J_\perp/J = 0$.** The lines show the results of a free-fermion simulation for system sizes 50 and 250 evaluated in a central ROI of 40 sites, both for no disorder and for white noise disorder of amplitude $\Delta = J$. Note that in the large system of 250 sites (that is not affected by finite system size effects for the times shown) the variance grows almost up to the theory prediction $\approx L/2$. Both finite system size effects and disorder lead to a reduction in the variance growth and a smaller saturation value.

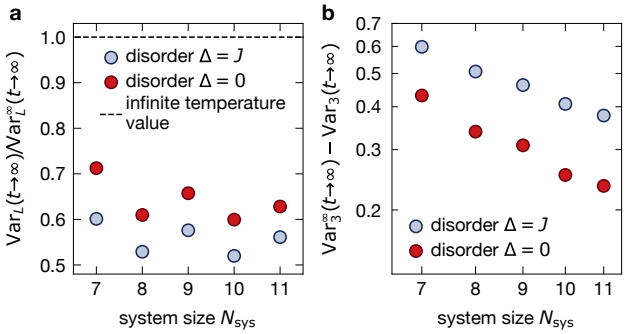

Figure S11. **Fully coupled ladder small scale numerics.** The saturation value of fluctuations in simulations of small systems ($7 \leq N_{\rm sys} \leq 11$). $\mathrm{Var}_L^\infty(t)$ denotes the infinite temperature prediction. **a**, The (normalised) saturation value of the half-system number variance for different total system sizes, showing a robust suppression of fluctuations as system size is increased. **b**, The deviation of saturation value for the number variance from the infinite temperature value for a subsystem of size $L = 3$ at different total system sizes $7 \leq N_{\rm sys} \leq 11$. All simulations were carried out in the hard-core limit $U \to \infty$.

amplitude $\Delta = J$, evaluated in a central ROI of 40 sites. Fig. S10 shows the time evolution of the atom number variance in a subsystem of size $L = 14$. Information about the edges propagates towards the centre ballistically with Lieb-Robinson velocity $4Ja/\hbar$, and ROI of size 40 inside a system of size 250 is therefore not affected by finite system size effects for the times shown in Fig. S10 ($t/T < 20$). We can see that in a clean system that is not affected by finite-size effects, the variance saturation value is reaching the theoretical prediction $\approx L/2$.

For a system size of 50 sites (realised in the experiment), we observe a clear reduction of the saturation value due to finite-size effects, both in the clean system and in the presence of disorder with an amplitude comparable to our experiment ($\Delta \sim J$). The combined effect of disorder and finite system size then leads to good agreement with the experimentally measured atom-number variances. In contrast to the subsystem variances, the local imbalance is not significantly affected by finite-size effects.

3. *Simulations of fully coupled ladders*

To investigate the effects of disorder and finite system size in the fully coupled ladder ($J_\perp/J = 1$), we numerically study this system (using MPS-TEBD simulations using the open-source package TeNPy [9]) for different system sizes. The rapidly entangling evolution of the fully coupled ladder limits us to small system sizes, with the number of rungs, $N_{\rm sys}$, at most $N_{\rm sys} = 11$ (i.e. 22 sites). In both the clean and disordered systems, we observe that large-scale fluctuations (fluctuations of observables of a large fraction of the system) fail to reach the infinite temperature value. In Fig. S11a, we show the number variance for subsystem size equal to half the total system size $L = \lfloor N_{\rm sys}/2 \rfloor$. This shows the half-system number variance remaining strongly suppressed from the thermal value as the system size is increased, even as expectation values thermalise.

If the opposite limit is taken, $N_{\rm sys} \to \infty$ with fixed subsystem size, we find evidence that the fluctuations do thermalise, as expected. Fig. S11b shows the deviation in saturation values from the infinite temperature value ($L/2$) for subsystem size $L = 3$ for different total system size. We see, in both the clean and disordered case, a power-law approach to the infinite temperature value as system size increases, with the disordered case having a more pronounced suppression.

In the experiment, we observe the saturation of fluctuations in subsystems up to 1/5 of the total system size and find a $\sim 20\%$ suppression of the number variance for these subsystem sizes (see Fig. S4). This is comparable to the reduction seen in the small-scale numerics for similarly sized subsystems (in proportion to the total system). For example, taking a subsystem of 3 rungs in a total system of 11 rungs, we find a reduction of $\sim 25\%$. We thus note that the finite-size effects can be relevant even in the case of a fully coupled ladder with diffusive correlation spreading.

D. Experimentally measured inhomogeneities

To characterise inhomogeneities in our superlattice potential that we use to generate the ladder systems, we

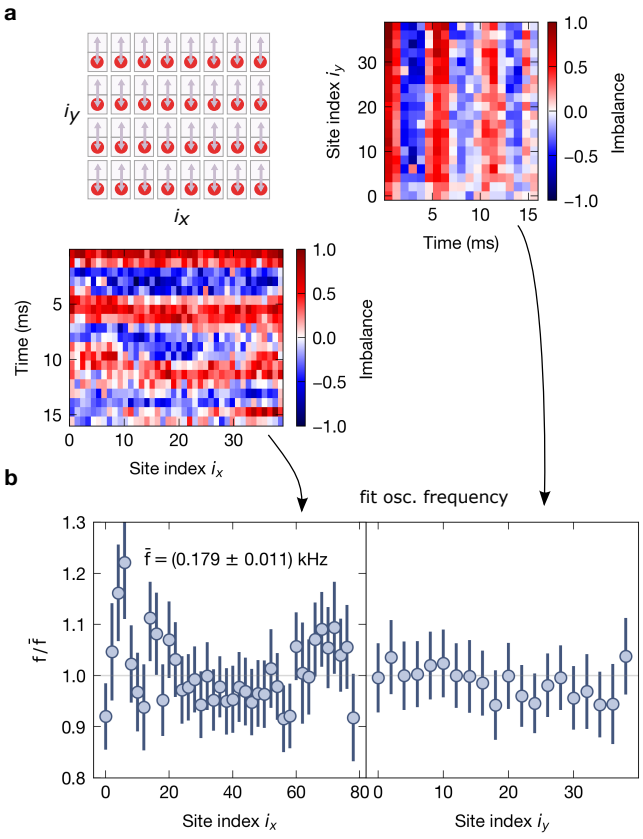

Figure S12. **Spatially resolved double well oscillations.** **a**, In order to quantify the homogeneity of the superlattice potential that we use to realise ladder systems, we observe oscillations in isolated double wells. The local time evolution of the imbalance is averaged along either the x- or the y-direction (i.e. along or perpendicular to the ladder, respectively, see 2a for definition of x and y) and **b**, fitted using a sine function to obtain the double well oscillation frequency as a function of position.

perform double-well oscillations by adiabatically preparing a CDW with each atom being localized in an isolated double well. Then, we quench on the tunnelling strength between the two sites of each double well and observe the atom oscillating between the two sites. Due to inhomogeneities within our ROI, some double wells will be more tilted than others, locally varying the double-well oscillation frequency. By measuring the spatial variation of this frequency in our ROI, we get a spatial profile of double well tilts in the superlattice potential. Fig. S12a shows the imbalance as a function of time, averaged along the columns and rows of our square superlattice. The imbalance can be seen oscillating at an average frequency of $\bar{f} = 179(11)\,\mathrm{Hz}$ with variations on the scale of 10% indicating double well tilts up to 30 Hz.

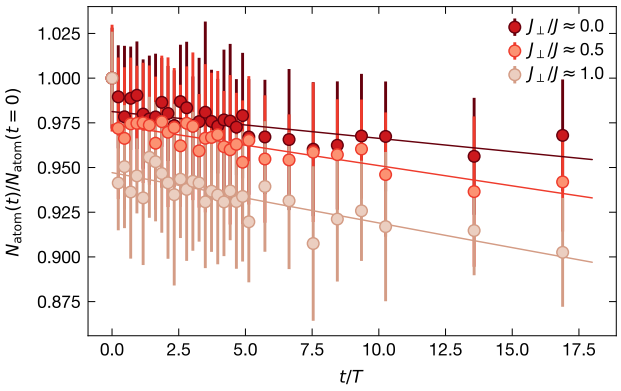

Figure S13. **Atom loss during the time evolution after the quench.** Fraction of remaining atoms (after parity projection) as a function of time, normalised to the initial state value at $t = 0$. The initial drop in the atom number for the case of a fully coupled ladder ($J_\perp/J \approx 1.0$) can be attributed to doublon generation.

E. Atom loss

During the time evolution, we experience atom loss as a result of heating of the atoms in the optical lattice. Furthermore, due to the finite interaction energy U, there is a small doublon fraction $\lesssim 3\,\%$ that gets parity projected during fluorescence imaging and reduces the number of visible atoms. The latter effect is enhanced in the ladder case ($J_\perp/J \approx 1.0$), where U/J is smaller (but still in the hard-core limit). As shown in Fig. S13, the total atom loss remains below 10 % throughout the time evolution and does not have a significant impact on our results.

IV. FLUCTUATING HYDRODYNAMICS OF DIFFUSIVE QUANTUM SYSTEMS

In this section, we derive hydrodynamic formulas for the equal-time correlations and the atom number transfer variance after a quench from a fully polarized charge density wave state. We also adapt this to imperfect initial states. We will assume that the dynamics of particle density is decoupled from the energy density at half-filling and infinite temperature.

This assumption is justified since at half filling, particle-hole symmetry (in the hard-core limit) excludes a thermoelectric coupling in linearised hydrodynamics – the coupling must enter non-linearly, through the transport coefficients $D(\varepsilon, n)$. Moreover, at infinite temperature, $\varepsilon \to -\varepsilon$ symmetry forces the energy density to enter quadratically in D, $D(\varepsilon, n) \sim D(n) + \mathcal{O}(\varepsilon^2)$. This weak coupling between the two modes gives sub-leading $1/\sqrt{t}$ corrections to the hydrodynamics of a single diffusive density mode. In the following, we will assume that these modes are decoupled. A further simplification is to assume a constant diffusion coefficient D, which we

take to be the infinite temperature half-filling diffusion constant. This assumption is reasonable as: (1) the initial CDW state rapidly equilibrates to a constant density on average ($\overline{n} = 1/2$), and (2) the diffusion constant is both analytic and weakly dependent on density and temperature around the half-filled infinite temperature state [10].

The resulting description of the particle density in the chaotic ladder is a constant D noisy diffusion equation (see Eq. (2) in the main text). This equation is known to describe the hydrodynamics of a symmetric simple exclusion process [11], and was also recently shown to describe the hydrodynamics of fluctuations in number-conserving random unitary circuit models [12]. Rather than work with the fluctuating hydrodynamic equation directly (which has only been solved in equilibrium and for domain-wall states [11]), we will use an operator growth ansatz for the Heisenberg evolution of particle density consistent with diffusive hydrodynamics (following Ref. [13]).

A. Equal-time density-density correlations

In this section, we provide a theory for density-density correlations in chaotic systems at half-filling shown in equation (S9), which includes the CDW initial state and the infinite temperature state. We will find it helpful to use a shorthand notation $\xi = (\alpha, i)$ to label both the leg α and rung i of the ladder, as well as to define charge operators $\hat{z}_\xi = 2\hat{n}_\xi - \mathbb{1}$, which measure the deviation in the occupancy from half-filling on a given site. For a fully coupled ladder, charge will spread diffusively, quickly equilibrating between the legs, whereas longer wavelength hydrodynamic modes will describe the dynamics of charge along the extended direction (along the legs of the ladder) – charge will spread with a width $\sqrt{2Dt/a^2}$. For concreteness, we assume a Gaussian kernel for the spreading of charge,

$$\mathrm{Tr}(\hat{z}_\xi(t)\hat{z}_\eta)/\mathrm{Tr}(\mathbb{1}) = K_{\xi,\eta}(t) \equiv \frac{1}{2}\frac{a\, e^{-\frac{(i-j)^2 a^2}{4Dt}}}{\sqrt{4\pi D t}}, \quad \text{(S15)}$$

where a is the lattice spacing, and where the factor of $1/2$ is due to the ladder geometry (charge can be on either site of a rung). Under Heisenberg operator evolution, the charges can also develop overlap with products of many local charge densities, as well as non-diagonal (and therefore non-hydrodynamic) operators not captured by equation (S15). Diffusive hydrodynamics places general restrictions on this operator growth [13], bounding the coefficients in an operator expansion of Heisenberg-evolved densities.

These higher-order terms can be regarded either through the perspective of Heisenberg operator growth or as consequences of integrating over the noise. The Heisenberg-evolved density $\hat{z}_\xi(t)$ admits the operator expansion

$$\hat{z}_\xi(t) = \sum_{\xi'} K_{\xi,\xi'}(t)\hat{z}_{\xi'} + \sum_{n\geq 2}\sum_{\xi_1<\cdots<\xi_n} B^{(n)}_{\xi,(\xi_1,\cdots\xi_n)}(t)\hat{z}_{\xi_1}\cdots\hat{z}_{\xi_n} + \cdots . \quad \text{(S16)}$$

The coefficients $B^{(n)}(t)$ decay faster than $K(t)$ (the coefficients $B^{(n)}(t)$ decay as $t^{-3/2}$ in $U(1)$ random unitary circuits [13]), and where the ellipsis denotes non-diagonal terms. This describes the diffusive dynamics of a single charge operator. As the density-density two-point function involves a product of charges, we must also write a similar expression for the Heisenberg evolution of a pair of charge operators $\hat{z}_\xi(t)\hat{z}_\eta(t)$, $\xi \neq \eta$. Showing only the slowest hydrodynamic mode, $zz \to zz$, in which the two charges undergo single-file diffusion (and do not generate or annihilate further charges), we have

$$\hat{z}_\xi(t)\hat{z}_\eta(t) = \sum_{\xi',\eta'} K_{(\xi,\eta),(\xi',\eta')}(t)\hat{z}_{\xi'}\hat{z}_{\eta'} + \cdots . \quad \text{(S17)}$$

The kernel $K_{(\xi,\eta),(\xi',\eta')}(t)$ must vanish at $\xi' = \eta'$ as much like a single charge, products of charge operators can never develop overlap with the identity operator. For diagonal (in number basis) ρ, all non-diagonal terms in the operator expansion vanish. By neglecting slower hydrodynamic contributions, which involve transmuting one z-string to another by the creation or annihilation of z's, we are assuming a linearised hydrodynamic description. Under this assumption, the connected equal-time charge-charge correlator (with $\xi \neq \eta$) is given by

$$\begin{aligned}\langle \hat{z}_\xi \hat{z}_\eta \rangle^C_{\rho(t)} &\equiv \langle \hat{z}_\xi \hat{z}_\eta \rangle_{\rho(t)} - \langle \hat{z}_\xi \rangle_{\rho(t)} \langle \hat{z}_\eta \rangle_{\rho(t)} \\ &= \sum_{\xi,\eta} \Big(K_{(\xi,\eta),(\xi',\eta')}(t) \langle \hat{z}_{\xi'}\hat{z}_{\eta'} \rangle_\rho \\ &\quad - K_{\xi,\xi'}(t) K_{\eta,\eta'}(t) \langle \hat{z}_{\xi'} \rangle_{\rho_0} \langle \hat{z}_{\eta'} \rangle_{\rho_0} \Big) . \end{aligned} \quad \text{(S18)}$$

The $zz \to zz$ kernel decouples at late times (the contact interactions of random walkers is RG irrelevant [12], leading to a faster decay $\delta K \sim t^{-2}$),

$$\begin{aligned} K_{(\xi,\eta),(\xi',\eta')}(t) = \frac{1}{2}\left(K_{\xi,\xi'}(t)K_{\eta,\eta'}(t) + K_{\xi,\eta'}(t)K_{\eta,\xi'}(t)\right) \\ + \delta K_{(\xi,\eta),(\xi',\eta')}(t). \end{aligned} \quad \text{(S19)}$$

Using this, and the fact that $\langle \hat{z}_{\xi'}\hat{z}_{\eta'} \rangle_\rho = \langle \hat{z}_{\xi'} \rangle_\rho \langle \hat{z}_{\eta'} \rangle_\rho$ for $\xi' \neq \eta'$, we write

$$\begin{aligned} \langle \hat{z}_\xi \hat{z}_\eta \rangle^C_{\rho(t)} = \sum_{\xi'} K_{\xi,\xi'}(t)K_{\eta,\xi'}(t)(1 - \langle \hat{z}_{\xi'} \rangle^2_\rho) \\ + \sum_{\xi',\eta'} \delta K_{(\xi,\eta),(\xi',\eta')}(t) \langle \hat{z}_{\xi'}\hat{z}_{\eta'} \rangle_\rho . \end{aligned} \quad \text{(S20)}$$

The correction δK to the $zz \to zz$ kernel results from scattering events of two 'hard-core' random walkers. For

a scattering of z's with initial positions ξ and η and final positions ξ' and η' to occur, the z's must diffuse until next to one another, scatter, and then diffuse to their final positions. Such a process is exponentially suppressed in the (scaled) separations $(i-j)/\sqrt{Dt/a^2}$, $(i'-j')/\sqrt{Dt/a^2}$, and the (scaled) centre of mass separation $(\frac{i+j}{2}-\frac{i'+j'}{2})/\sqrt{Dt/a^2}$. For states with density variations on length scales, much smaller than $\sqrt{Dt/a^2}$, δK and K vary much more slowly than $\langle \hat{z}_{\xi'}\rangle_\rho$ and $\langle \hat{z}_{\xi'}\rangle_\rho^2$. We are therefore able to replace these with their spatial averages, $\langle \hat{z}_{\xi'}\rangle_\rho \to 2\overline{n}-1$ and $\langle \hat{z}_{\xi'}\rangle_\rho^2 \to 1-4\langle \mathrm{Var}(\hat{n}_\xi)\rangle_\xi$. Putting this into equation (S20) yields

$$\langle \hat{z}_\xi \hat{z}_\eta\rangle^C_{\rho(t)} = \sum_{\xi'} 4\langle \mathrm{Var}(\hat{n}_\xi)\rangle_\xi K_{\xi,\xi'}(t), K_{\eta,\eta'}(t) + \sum_{\xi',\eta'} \delta K_{(\xi,\eta),(\xi',\eta')}(t)(\delta_{\xi',\eta'} + \delta_{\xi'\neq\eta'}(2\overline{n}-1)^2). \tag{S21}$$

Together with the sum rules for $K_{(\xi,\eta),(\xi',\eta')}(t)$ and $K_{\xi,\xi'}(t)$, the condition that $K_{(\xi,\eta),(\xi',\xi')}(t)=0$ yields $\delta K_{(\xi,\eta),(\xi',\xi')}(t) = -K_{\xi,\xi'}(t)K_{\eta,\xi'}(t)$. Altogether, we find

$$\langle \hat{z}_\xi \hat{z}_\eta\rangle^C_{\rho(t)} = 4(\langle \mathrm{Var}(\hat{n}_\xi)\rangle_\xi - \chi(\overline{n}))K_{\xi,\eta}(2t) + 4\chi(\overline{n})\delta_{\xi,\eta}, \tag{S22}$$

where we fixed the value of the correlator at $\xi=\eta$ using similar arguments to those presented in the above for $\xi\neq\eta$. Converting back to number operators $\hat{n}_{\alpha,i}$, the equal-time density-density correlator is given by equation (S9), as required.

B. Counting statistics of number transfer

The number of atoms $\mathcal{N}$ transferred in and out of an ROI labeled S is a stochastic variable, its variance can be related to the two-time and equal-time density-density correlators (see SM Section II B) as follows,

$$\mathrm{Var}(\mathcal{N}(t)) = \sum_{(\alpha,i),(\beta,j)\in S} \Big[C^{\alpha,\beta}_{i,j}(t) - 2\langle \hat{n}_{\alpha,i}(t)\hat{n}_{\beta,j}(0)\rangle + 2\langle \hat{n}_{\alpha,i}(t)\rangle\langle \hat{n}_{\beta,j}(0)\rangle + C^{\alpha,\beta}_{i,j}(0)\Big]. \tag{S23}$$

For an initial state with a sharp number of atoms in the ROI, the connected two-time functions are zero, enabling us to reconstruct the FCS from the equal-time correlators alone. Using equation (S9) for the density-density correlator, we find the following prediction for the atom transfer variance across the central bond of the ladder for a fully polarised charge density wave state (in which all sites on even bonds are fully occupied and all sites on odd bonds are empty),

$$\mathrm{Var}(\mathcal{N}(t))_{\mathrm{CDW}} \approx \sqrt{\frac{Dt}{2\pi\, a^2}}. \tag{S24}$$

We have checked that this formula also holds for classical stochastic systems such as the simple symmetric exclusion process [11, 14]. This is easily adapted for finite subsystems with two boundaries through which atoms can transfer. For a subsystem of length L, the variance of atom number transfer grows at twice the rate of the subsystem with a single boundary until fluctuations equilibrate to the infinite temperature half-filling value ($\mathrm{Var}(\mathcal{N}_L)\to L/2$) at times $t\sim (La)^2/D$,

$$\mathrm{Var}(\mathcal{N}_L(t))_{\mathrm{CDW}} \approx \sqrt{\frac{2Dt}{\pi\, a^2}}, \quad t\ll (La)^2/D. \tag{S25}$$

In the absence of two-time correlation data, and with initial state imperfections (leading to a loss of sharpness in atom number), we must modify this and instead look at the growth of variance of subsystem atom number, $\mathrm{Var}_L(t)-\mathrm{Var}_L(0)$. Using equation (S9) for the equal-time correlators, we find

$$\mathrm{Var}_L(t)-\mathrm{Var}_L(0) \approx 4(\chi - \langle \mathrm{Var}(\hat{n}_{\alpha,i})\rangle_{\alpha,i})\sqrt{\frac{2Dt}{\pi\, a^2}}, \tag{S26}$$

for times $t\ll (La)^2/D$, and where $\chi=\overline{n}(1-\overline{n})=1/4$ is the susceptibility at half filling ($\overline{n}=0.5$), and $\langle \mathrm{Var}(\hat{n}_{\alpha,i})\rangle_{\alpha,i}$ is the number variance on a single site in the initial state, averaged over sites. We use equation (S26) to fit the experimental data in Fig. 3d with free fit parameters D and $\mathrm{Var}_L(0)$.

C. Notes on integrable and chaotic regimes

In this section, we briefly review some standard results and theoretical expectations on transport in the XX ladder. At asymptotically late times, this model is believed to be chaotic for all values of $J_\perp/J$ other than 0 and ∞. When $J_\perp=0$, as discussed in the main text, the model maps to free fermions. For $0<J_\perp/J\ll 1$, the dynamics resembles that of free fermions for a long time, but eventually crosses over to chaotic diffusive transport. The associated crossover timescale t_* is given by Fermi's Golden Rule, and scales as $t_* J\sim (J/J_\perp)^2$. In the opposite limit, $J_\perp/J\gg 1$, one solves the problem by first diagonalizing each rung of the ladder. This gives a system of interacting fermions with two bands split by the scale $J_\perp$. Fermions in distinct bands are distinguishable and interact via contact interactions. The number of fermions in each band is strictly conserved in the limit $J_\perp\to\infty$; when $J_\perp/J\gg 1$, this emergent conservation law holds up to timescales $\sim \exp(J_\perp/J)$. This exponential timescale is a consequence of prethermalization. In both regimes $J_\perp/J\ll 1, J_\perp/J\gg 1$, the hydrodynamic regime we are interested in only sets in at late times, which are not experimentally accessible. To reach the hydrodynamic regime on experimentally relevant timescales, we choose to work at $J_\perp=J$.

D. Fluctuation growth in other models

In this section, we provide additional numerical evidence that the growth of fluctuations in chaotic quantum systems is indeed governed by fluctuating hydrodynamics. Because late-time simulations of chaotic quantum systems are generally intractable even for the most modern numerical methods, we are forced to study noisy systems, in which the noise (implemented as a dephasing channel as in Ref. [15]) prevents the boundless growth of complexity that occurs in noiseless systems. In this setting, we can simulate the dynamics out to late times and make direct comparisons of fluctuation growth far from equilibrium with the equilibrium diffusion constant, testing the prediction (equation (3)) of fluctuating hydrodynamics.

We simulate a noisy staggered-anisotropy XXZ chain with Hamiltonian $H = H_0 + V(t)$, where the noise is coupled to the z-component of spin $V(t) = \sum_j \eta_j(t) S^z_j$, and is uncorrelated in space and time $\langle \eta_i(t)\eta_j(t')\rangle = \gamma\delta_{i,j}\delta(t-t')$. The noiseless Hamiltonian H_0 is given by

$$H_0 = \sum_j \left(X_jX_{j+1} + Y_jY_{j+1} + \Delta Z_jZ_{j+1}\right) + J_{\text{stag}} \sum_j (-1)^j Z_{j+1}, \tag{S27}$$

where X_i, Y_i, Z_i denote Pauli matrices on site i. We look at three different Hamiltonians H_0 with various noise strengths: (1) $\Delta = 1, J_{\text{stag}} = 0$ is the isotropic Heisenberg model, the equilibrium diffusion constant was previously studied in the noisy case in Ref. [15]; (2) $\Delta = 0.5, J_{\text{stag}} = 0.5$, this model is chaotic with diffusive magnetisation transport [16]; (3) $\Delta = 0.25, J_{\text{stag}} = 0.25$, this is yet another chaotic diffusive model. We use matrix product states and the time-evolving-block-decimation algorithm for our simulations (using the open-source package TeNPy [9]). In our simulations, we set a system size of $L = 60$ and fix a maximum bond dimension of $\chi = 350$ that is sufficient for converged (numerically obtained) diffusion coefficients.

For the equilibrium linear-response evaluation of the diffusion constant, we evolve a single Z_j operator at the centre of the system $j = 0$, and compute the two-point functions $C_{0,j}(t) = \langle Z_0(t)Z_j\rangle$. We set the lattice spacing $a = 1$ and compute the mean-square displacement $\text{MSD}(t) = \sum_j j^2 C_{0,j}(t) - \left(\sum_j jC_{0,j}(t)\right)^2$ which allows for the determination of a time-dependent diffusion coefficient $D_{\text{eq}}(t) = \frac{1}{2}\frac{d}{dt}\text{MSD}(t)$. For large noise strength γ, $D(t)$ plateaus quickly to the true diffusion constant $D \equiv D(\infty)$ as shown in Fig. S14.

For the far-from-equilibrium determination of the diffusion constant, we evolve a Néel state (the one-dimensional chain equivalent of the ladder CDW in our experiment) and compute the variance of charge transfer across the central bond of system, $\text{Var}(\mathcal{N}(t))_{\text{Néel}}$. Changing a ladder geometry for a one-dimensional chain, we must replace Eq. (S24) for the growth of charge transfer variance with $\text{Var}(\mathcal{N}(t))_{\text{Néel}} \approx \sqrt{Dt/8\pi\, a^2}$. Using this, we define the time-dependent diffusion coefficient as follows,

$$D_{\text{Néel}}(t) = 8\pi \frac{d}{dt}\text{Var}(\mathcal{N}(t))^2_{\text{Néel}}. \tag{S28}$$

In Fig. S14, we have shown $D_{\text{eq}}(t)$ and $D_{\text{Néel}}(t)$ for each of the three choices of H_0, and for noise strengths $\gamma = 0.05, 0.1, 0.2$. In each case, we find that the time-dependent $D_{\text{Néel}}(t)$ approaches the equilibrium value. While $D_{\text{Néel}}(t)$ is seen to approach the equilibrium value at long times, over the simulation times we have accessed here, this final plateau is not always reached. Therefore, our best estimate for $D_{\text{Néel}}(\infty)$ is to take $D_{\text{Néel}}(t)$ at the final simulated time. The equilibrium linear response estimates for D, and the best estimates from the Néel state fluctuation growth are summarised in the table below.

$\Delta = 1.00,\ J_{\text{stag}} = 0.00$:	γ	0.05	0.1	0.2
	D_{eq}	0.914	0.671	0.439
	$D_{\text{Néel}}$	0.913	0.656	0.463
$\Delta = 0.50,\ J_{\text{stag}} = 0.50$:	γ	0.05	0.1	0.2
	D_{eq}	0.599	0.492	0.378
	$D_{\text{Néel}}$	0.604	0.514	0.397
$\Delta = 0.25,\ J_{\text{stag}} = 0.25$:	γ	0.05	0.1	0.2
	D_{eq}	1.383	0.888	0.524
	$D_{\text{Néel}}$	1.418	0.926	0.554

For each H_0 and noise strength γ, the best estimate of $D_{\text{Néel}}(\infty)$ lies within 6% of the equilibrium value. These results, together with our experimental results for fluctuation growth in a Bose-Hubbard ladder, demonstrate that far-from-equilibrium fluctuation growth is a quantitative probe of equilibrium transport.

SUPPLEMENTARY REFERENCES

[1] T. Klostermann, C. R. Cabrera, H. von Raven, J. F. Wienand, C. Schweizer, I. Bloch, and M. Aidelsburger, Phys. Rev. A **105**, 043319 (2022).

[2] A. Impertro, J. F. Wienand, S. Häfele, H. von Raven, S. Hubele, T. Klostermann, C. R. Cabrera, I. Bloch, and M. Aidelsburger, arXiv:2212.11974.

[3] S. Fölling, S. Trotzky, P. Cheinet, M. Feld, R. Saers, A. Widera, T. Müller, and I. Bloch, Nature **448**, 1029 (2007).

[4] S. Trotzky, Y.-A. Chen, A. Flesch, I. P. McCulloch, U. Schollwöck, J. Eisert, and I. Bloch, Nat. Phys. **8**, 325 (2012).

[5] A. Impertro, S. Karch, J. F. Wienand, S. Huh, C. Schweizer, I. Bloch, and M. Aidelsburger, Local readout and control of current and kinetic energy operators in optical lattices (2023).

[6] L. W. Cheuk, M. A. Nichols, M. Okan, T. Gersdorf, V. V. Ramasesh, W. S. Bakr, T. Lompe, and M. W. Zwierlein, Phys. Rev. Lett. **114**, 193001 (2015).

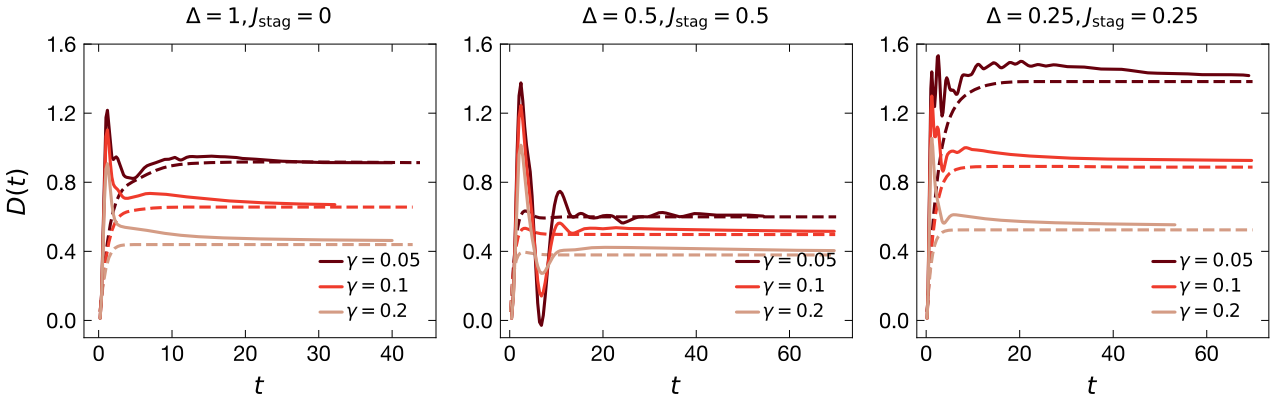

Figure S14. **Diffusion constant from far-from-equilibrium fluctuations.** We compute a time-dependent diffusion constant from equilibrium linear response (dashed) and from the growth of charge transfer variance via equation (3). We do this for a staggered-anisotropy XXZ model (equation (S27)) at three different parameter choices: $\Delta = 1$, $J_{\text{stag}} = 0$ (panel 1), this model is integrable in the noiseless limit, but chaotic and diffusive in the presence of noise [15] (panel 1); $\Delta = 0.5$, $J_{\text{stag}} = 0.5$ (panel 2); and $\Delta = 0.25$, $J_{\text{stag}} = 0.25$ (panel 3). (The models in panels 2 and 3 are chaotic and diffusive even at zero noise.)

[7] A. Smith, *Disorder-Free Localization*, 1st ed. (Springer, 2019).

[8] A. H. Karamlou, J. Braumüller, Y. Yanay, A. Di Paolo, P. M. Harrington, B. Kannan, D. Kim, M. Kjaergaard, A. Melville, S. Muschinske, B. M. Niedzielski, A. Vepsäläinen, R. Winik, J. L. Yoder, M. Schwartz, C. Tahan, T. P. Orlando, S. Gustavsson, and W. D. Oliver, NPJ Quantum Inf. **8**, 35 (2022).

[9] J. Hauschild and F. Pollmann, SciPost Phys. Lect. Notes (2018).

[10] R. Steinigeweg, F. Heidrich-Meisner, J. Gemmer, K. Michielsen, and H. De Raedt, Phys. Rev. B **90**, 094417 (2014).

[11] K. Mallick, H. Moriya, and T. Sasamoto, Phys. Rev. Lett. **129**, 040601 (2022).

[12] E. McCulloch, J. De Nardis, S. Gopalakrishnan, and R. Vasseur, Phys. Rev. Lett. **131**, 210402 (2023), arXiv:2302.01355 [quant-ph].

[13] C. von Keyserlingk, F. Pollmann, and T. Rakovszky, Phys. Rev. B **105**, 245101 (2022).

[14] B. Derrida and A. Gerschenfeld, J. Stat. Phys. **136**, 1 (2009).

[15] J. De Nardis, S. Gopalakrishnan, R. Vasseur, and B. Ware, Phys. Rev. Lett. **127**, 057201 (2021), arXiv:2102.02219 [cond-mat.stat-mech].

[16] Y. Yoo, C. D. White, and B. Swingle, Phys. Rev. B **107**, 115118 (2023), arXiv:2210.06494 [cond-mat.str-el].